



Secondary electron imaging at atomic resolution using a focused coherent electron probe

H. G. Brown, A. J. D'Alfonso, and L. J. Allen*

School of Physics, University of Melbourne, Parkville, Victoria 3010, Australia

(Received 3 December 2012; published 5 February 2013)

Atomic resolution imaging using secondary electrons (emitted as a result of the interaction of incident fast electrons with a specimen) was only achieved recently. There has been considerable speculation as to the physical mechanisms underpinning the imaging. In this paper we use a quantum mechanical model to show that the image contrast is due to electrons ejected in inner-shell ionization events initiated by the primary beam, an atomic scale, and focused coherent electron probe. The angular probability distribution of the ejected electrons is key in understanding the (relative) contrast from different atomic species within the specimen. For a given species of atom, this angular probability distribution is predominantly determined by the angular momentum quantum number of the bound electron prior to ionization. The model is compared to experiment and reproduces the essential features in the data.

DOI: [10.1103/PhysRevB.87.054102](https://doi.org/10.1103/PhysRevB.87.054102)

PACS number(s): 61.05.jd

I. INTRODUCTION

Electron microscopy allows imaging of single atoms¹ and sub-Ångström mapping of elements in a crystal lattice.^{2,3} The advent of spherical aberration correction for electron microscope lenses has meant that many of the techniques commonly used in electron microscopy can now more easily resolve individual atomic columns and resolve them at lower accelerating voltages.⁴ In scanning transmission electron microscopy, the techniques of annular dark field imaging, electron energy loss spectroscopy, and, more recently, energy dispersive x-ray imaging provide atomic resolution imaging. In the area of scanning electron microscopy using secondary electrons this has been more elusive, the first atomic resolution images only being demonstrated as recently as 2009.⁵

As early as 1995, Howie⁶ addressed possible mechanisms for the “high spatial resolution frequently observed in SE [secondary electron] images.” He concluded that this is “adequately accounted for by the significant and often dominant contribution made by high momentum transfer, and hence well localized, excitation events in the initial generation process.” Consistent with this will be our assumption that the secondary electrons responsible for image contrast are assumed to have been generated by inner-shell ionization events, which are sufficiently localized to provide atomic resolution information. More recently, Inada *et al.*⁷ discussed, in broad terms, possible mechanisms by which atomic scale contrast in secondary electron images might be formed. A subsequent paper by Wu *et al.*⁸ introduced a model which took into account the channeling and thermal scattering of the probe and which used an object function model for the secondary electrons based on a simple model for inelastic scattering.

Secondary electron imaging is a routinely used technique and the relative ease and simplicity associated with operating a scanning electron microscope means that it finds wide application in both research and industry. The uses of modern scanning electron microscopes range from the imaging of biological specimens to the characterization of nanoscale silicon devices.⁹ It is the last of these which is perhaps one of the most important uses of the scanning electron microscope and with semiconductor device sizes becoming increasingly smaller, demands on the resolution of scanning electron

microscopes are increasing.¹⁰ In scanning electron microscopy a beam of electrons is accelerated using an applied voltage and finely focused down to a point on the specimen of interest. Unlike scanning *transmission* electron microscopy, where the image is built up by detecting transmitted primary electrons which have been both elastically and inelastically scattered, the secondary electron imaging detects electrons which have been generated by the incident fast electrons. Unlike other techniques in electron microscopy, secondary electron imaging has only recently been able to achieve atomic resolution imaging⁵ despite previous attempts with modern aberration corrected probes.¹¹ Using a 200-keV aberration corrected probe, Zhu *et al.*⁵ were able to demonstrate secondary electron imaging of single uranium atoms within a uranium oxide nanocrystal and columns of atoms within a $\text{YBa}_2\text{Cu}_3\text{O}_{7-x}$ (YBCO) superconducting crystal. Zhu *et al.* attributed the experimental advance primarily to the aberration correction of the electron probe and also to the improved stability of the electrooptical components of the microscope.

Consider a surface of a specimen (which we refer to as the entrance surface) irradiated by primary fast electrons (energy of the order of 100 keV). Electrons are then emitted from the entrance surface. Electrons with energies less than around 50 eV are the secondary electrons to which we refer.¹² Electrons with energies between around 50 eV and the energy of the incident electrons are mainly Auger electrons and thermally (Rutherford) backscattered electrons.¹² In the experiment of Zhu *et al.*⁵ the electrons that had a kinetic energy between 0 and 50 eV comprised 85–90% of those emitted in the backwards direction, with most having an energy less than 10 eV. In this paper, we model these low-energy electrons as being predominantly the product of inner-shell ionization events which, for an atomically sized probe, provide the high resolution information regarding atomic column positions.

As the majority of the secondary electrons have relatively low kinetic energies the secondary electrons have a high cross section for interaction with the crystal. This translates to a very short inelastic mean free path and consequently the probability of absorption into the crystal is large. It follows that most of the secondary electrons generated through ionization events within the crystal will only escape if they are emitted

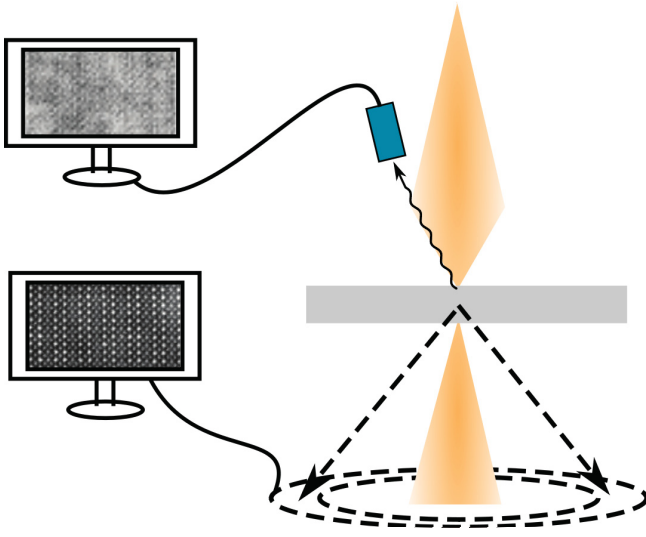


FIG. 1. (Color online) The experimental geometry of simultaneous secondary electron imaging and annular dark-field imaging. The secondary electrons are detected in the backwards direction and thermally scattered electrons in the annular dark-field detector in the forward direction. The secondary electron and annular dark-field images are from Zhu *et al.* (Ref. 5).

within a few Ångströms of the crystal surface.⁶ This property implies that secondary electron imaging is a good technique for imaging surfaces. Zhu *et al.*⁵ demonstrated the low penetration power of electrons produced by ionization events by placing a thin carbon film (around 2-nm thick) above a holey carbon film (around 20-nm thick). It was shown that the thin carbon film was sufficient to prevent the transmission of secondary electrons. These results imply that when a secondary electron image is recorded, the image will only reveal information near the surface.^{5,6,12} The set up of a modern secondary electron imaging instrument, such as the one used by Zhu *et al.*, and shown schematically in Fig. 1, allows an annular dark-field detector to be placed below the specimen so that annular dark-field microscopy may be performed in parallel to the secondary electron imaging measurement. This means that secondary electron imaging can provide surface imaging of the specimen while annular dark-field imaging gives information about atom column positions within the bulk of the crystal.⁵

Traditionally, the simulation of secondary electron images has relied on Monte Carlo methods which, while highly successful at lower energies and resolutions, are likely to be tested for an atomic-scale, focused coherent probe. Possible mechanisms for nanoscale secondary electron imaging have been discussed previously.⁶⁻⁸ Here we develop a quantum mechanical approach to secondary electron imaging based on the assumption that image contrast can be understood by considering inner-shell ionization. The model takes into account the elastic and inelastic scattering of the probe. Our model accounts for the directions in which electrons are ejected after the ionization of an atom and this is found to be important in simulating image contrast. Our approach places atomic resolution secondary electron imaging onto a firm theoretical footing and the insights developed allow a better understanding of the mechanisms that produce contrast in

secondary electron images and what physical factors affect the imaging. Results simulated using this approach are compared to the experimental results of Zhu *et al.*⁵

II. SIMULATING SECONDARY ELECTRON IMAGING

In Monte Carlo methods incident electron trajectories are treated semiclassically and simulations proceed by tracking electrons as they scatter through the specimen, calculating the probability of the production of secondary and thermally backscattered electrons in the process.^{13,14} Monte Carlo simulations have achieved a good fit to experiment for low probe accelerating voltages (usually between 200 and 30 keV)^{14,15} and make it clear that the observed image delocalization, which is greater than the size of the probe, occurs due to the inelastic scattering of the incident electrons.

The delocalization of the signal due to multiple inelastic scattering of the probe is a possible reason for the failure of previous attempts at atomic resolution secondary electron imaging using a low-energy aberration corrected electron probe.¹¹ At higher incident energies, for example, the 200-kV probe used by Zhu *et al.*,⁵ this effect will be substantially reduced. We will use a quantum mechanical model which takes into account multiple elastic scattering and single inelastic scattering by the crystal to model ionization by a focused coherent probe.

A. Triple-differential cross section

The basis for our model is the triple differential cross section for the ionization of a single atom, with the pertinent kinematics shown schematically in Fig. 2. The incident electron has wave vector \mathbf{k} . After ionization the incident electron is scattered by an angle $\theta_{k'}$ from its original direction and now has wave vector \mathbf{k}' . The secondary electron is ejected from the atom with wave vector $\boldsymbol{\kappa}$ at an angle θ_{κ} from the direction of the incident electron. The conservation of energy can be written as $E_k = E_{k'} + E_{\kappa} + E_T$, where E_T is the ionization threshold energy. The conservation of momentum in the interaction, in the reference frame of the ionized atom, is given by $\mathbf{k} + \mathbf{p} = \boldsymbol{\kappa} + \mathbf{k}'$, where \mathbf{p} is the momentum of the electron while in its initial bound state.¹⁶ The momentum

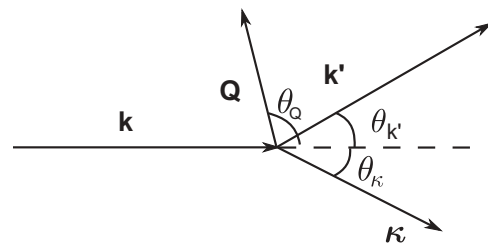


FIG. 2. Scattering kinematics for ionization of a single atom. An incident electron (plane wave) of wave vector \mathbf{k} is scattered to wave vector \mathbf{k}' . The ejected electron is emitted with wave vector $\boldsymbol{\kappa}$ and the wave vector transfer to the crystal is \mathbf{Q} . This representation of the ionization interaction is in free space for simplicity and clarity. In a crystalline environment conservation of momentum is defined up to a reciprocal lattice vector and this is taken into account in the calculations.

transfer is given by $h\mathbf{Q} = h\mathbf{k}' - h\mathbf{k}$, where h is Planck's constant.

Consider an atom contained in a slice of thickness t at a depth z in a crystal. The triple-differential cross section for the ionization of the atom by a fast electron incident on the crystal is given by¹⁷

$$\frac{d^3\sigma}{d\Omega_{k'}d\Omega_{\kappa}k'^2dk'} \Big|_{\mathbf{R}} = \frac{2\pi t}{h\nu} \int_A \int_A \phi_0^*(\mathbf{R}, \mathbf{r}_{\perp}, z) W(\mathbf{r}_{\perp}, \mathbf{r}'_{\perp}) \times \phi_0(\mathbf{R}, \mathbf{r}'_{\perp}, z) d\mathbf{r}_{\perp} d\mathbf{r}'_{\perp}. \quad (1)$$

Here $d\Omega_{k'}$ is the solid angle associated with the scattered electron after ionization. The ejected electron is scattered into a solid angle $d\Omega_{\kappa}$. The dependence of the cross section on the probe position \mathbf{R} is indicated. The velocity of the incident electron, with wave vector \mathbf{k} is given by $v = hk/m$, with m the relativistically corrected electron mass. The wave function of the probe in a plane perpendicular to the direction of propagation and at a depth z in the crystal is denoted by $\phi_0(\mathbf{R}, \mathbf{r}_{\perp}, z)$, where \mathbf{r}_{\perp} is a vector in that plane (as is \mathbf{r}'_{\perp}). The effective nonlocal scattering potential, projected and averaged over the distance t , can be expressed as a Fourier series

$$W(\mathbf{r}_{\perp}, \mathbf{r}'_{\perp}) = \sum_{\mathbf{g}, \mathbf{h}} W_{\mathbf{g}, \mathbf{h}} e^{2\pi i \mathbf{g} \cdot \mathbf{r}_{\perp}} e^{-2\pi i \mathbf{h} \cdot \mathbf{r}'_{\perp}}, \quad (2)$$

where the Fourier coefficients have the form¹⁷

$$W_{\mathbf{g}, \mathbf{h}} = \frac{2me^4}{16\pi^3 \epsilon_0^2 h^2 k' t} e^{-2\pi i (\mathbf{g} - \mathbf{h}) \cdot \boldsymbol{\tau}} \frac{F^*(\mathbf{Q}_{\mathbf{g}}, \kappa) F(\mathbf{Q}_{\mathbf{h}}, \kappa)}{|\mathbf{Q}_{\mathbf{g}}|^2 |\mathbf{Q}_{\mathbf{h}}|^2}. \quad (3)$$

Here e is the magnitude of the charge on an electron and ϵ_0 is the permittivity of free space. The vector $\boldsymbol{\tau}$ specifies the projected position of the atom relative to the origin of the unit cell. The vector $\mathbf{Q}_{\mathbf{g}} = \mathbf{Q} + \mathbf{g}$. The ionization form factor is given, in an angular momentum representation, by¹⁸

$$F(\mathbf{Q}, \kappa) = \frac{4\pi}{\kappa} \sum_{l'=0}^{\infty} \sum_{m_l'=-l'}^{l'} (-i)^{l'} e^{-i\delta_{l'}} Y_{l', m_l'}(\hat{\kappa}) \times \sum_{\lambda=0}^{\infty} \sum_{m_{\lambda}=-\lambda}^{\lambda} i^{\lambda} Y_{\lambda, m_{\lambda}}^*(\hat{\mathbf{Q}}) \int \frac{1}{r^2} u_{\kappa l'}(r) j_{\lambda}(2\pi Q r) \times u_{\nu l}(r) Y_{l', m_l'}^*(\hat{\mathbf{r}}) Y_{l, m_l}(\hat{\mathbf{r}}) Y_{\lambda, m_{\lambda}}(\hat{\mathbf{r}}) d\mathbf{r}. \quad (4)$$

The angular momentum and magnetic quantum numbers $\{l, m_l\}$ refer to the bound electron and $\{l', m_l'\}$ to the electron after it is ejected. The partial wave phase shift $\delta_{l'}$ is found by normalization to an asymptotic form for the ejected electron wave function.¹⁹ The Y_{l, m_l} are spherical harmonics and the j_{λ} are spherical Bessel functions. The radial wave function $u_{\kappa l'}(r)$ can be calculated by solving the Schrödinger equation using a Hartree-Slater potential.^{18,19} A partial wave component of the bound state wave function is denoted by $u_{\nu l}(r)$, calculated using a Hartree-Fock potential.¹⁹

In Figs. 3(a)–3(c) we show the polar plots of triple differential cross sections with respect to θ_{κ} , the ejection angle of the secondary electron, for K -shell ionization of carbon by 200-keV electrons with energies E_{κ} for the ejected electron of [Fig. 3(a)] 10, [Fig. 3(b)] 100, and [Fig. 3(c)] 1000 eV, for fixed $\theta_{k'} = 0$ and assuming plane wave illumination and $z = 0$ in Eq. (1). Of note is that the relative probability for emission

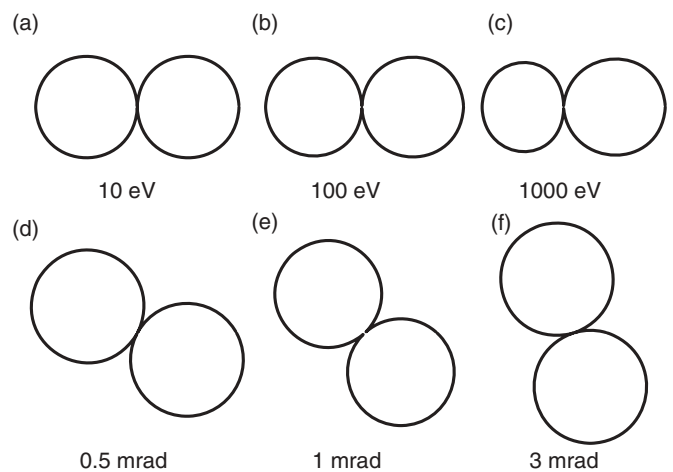


FIG. 3. Polar plots, for $\theta_{k'} = 0$, of triple-differential cross sections with respect to θ_{κ} , the ejection angle of the secondary electron, for K -shell ionization of carbon by 200-keV electrons with energies E_{κ} for the ejected electron of (a) 10, (b) 100, and (c) 1000 eV. The scattering angle $\theta_{k'}$ of the scattered fast electron is then varied over (d) 0.5, (e) 1.0, and (f) 3.0 mrad for the 10-eV case of part (a). In all of the above results the 200-keV primary electron is incident upon the carbon atom from the left and we have assumed plane wave illumination. The plots have their maxima normalized to unity.

in the backwards direction decreases as E_{κ} increases. The scattering angle $\theta_{k'}$ of the scattered fast electron is then varied over [Fig. 3(d)] 0.5, [Fig. 3(e)] 1.0, and [Fig. 3(f)] 3.0 mrad.

The rotation of the distributions in Figs. 3(d)–3(f) relative to that in Fig. 3(a) is worth exploring further. The cross section is symmetric about the direction of momentum transfer \mathbf{Q} . As $\theta_{k'}$ begins to increase \mathbf{Q} quite rapidly tilts off axis. We may readily, referring to Fig. 2, express the angle θ_Q in terms of $\theta_{k'}$ as

$$\theta_Q = \arcsin \left(\frac{k' \sin \theta_{k'}}{\sqrt{k^2 + k'^2 - 2kk' \cos \theta_{k'}}} \right) \quad (5)$$

and this function is plotted in Fig. 4. Clearly the angle θ_Q grows rapidly and becomes large for only small scattering angles $\theta_{k'}$. The results in Fig. 3 are normalized so that their maximum values are scaled to unity—we are mainly interested in the

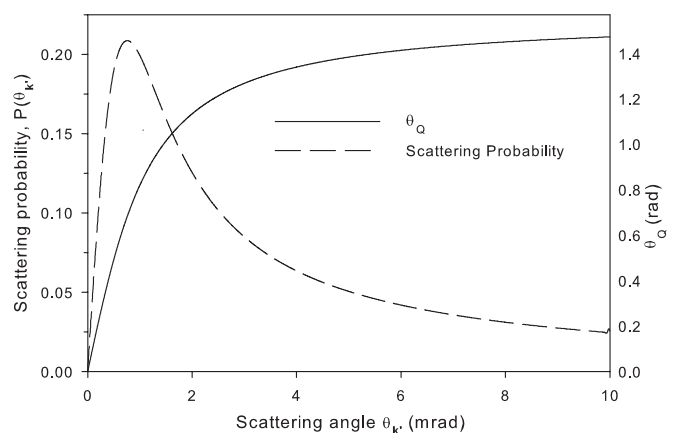


FIG. 4. θ_Q as a function of the scattering angle $\theta_{k'}$ plotted alongside the probability of scattering to this angle (arbitrary units).

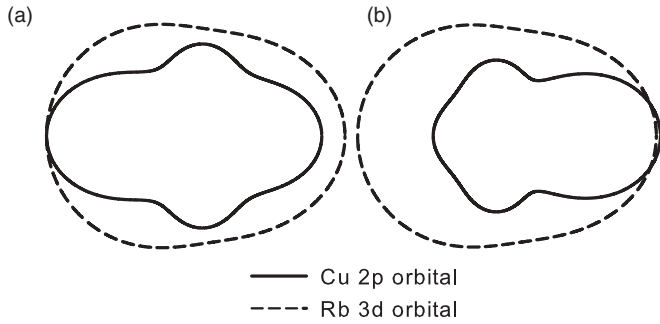


FIG. 5. The triple-differential cross section for ionization involving some electrons with the initial angular momentum quantum number $l \neq 0$ for (a) plane wave incidence and (b) a focused coherent probe with probe forming semi-angle $\alpha = 28$ mrad. In each case the 200-keV probe is incident from the left and the scattered electron is in the direction of $\theta_{k'} = 0$ mrad.

distributions as a function of angle. However, in reality the magnitude of the distributions varies as a function of energy loss and scattering angle. If we integrate the results such as those in Figs. 3(a) and 3(d)–3(f) over the full solid angle $d\Omega_{k'}$ then we obtain the second result shown in Fig. 4. This can be considered as the probability $P(\theta_{k'})$ for scattering through the angle $\theta_{k'}$. While most of the inelastic scattering of the fast electron is typically through small angles (between 0 and 5 mrad) θ_Q rapidly exceeds a radian, even for small values of $\theta_{k'}$. The observations in this paragraph will be pertinent later when we discuss Fig. 6(a).

Shown in Fig. 5 is the triple-differential cross section for ionization involving two different bound state electrons, copper 2*p* electrons and rubidium 3*d* electrons, using both [Fig. 5(a)] plane wave illumination and [Fig. 5(b)] an aberration free focused coherent probe with a 28-mrad convergence angle. The focused probe is modeled by summing over a large number of equally weighted transverse components, while a normally incident plane wave has no transverse components. The incoming plane wave or electron probe is incident from the left. It is evident that the triple-differential cross sections produced are very different from the $l = 0$ case in Fig. 3. The triple-differential cross sections are strongly dependent on the bound state quantum number l , more so than other parameters such as the atomic number of the atom or the principal quantum number n of the ionized electron. We note that for the Cu 2*p* orbital there is a transfer of probability of emission to the forward direction as one moves from plane wave incidence, shown in Fig. 5(a) to a focused coherent probe, shown in Fig. 5(b). Clearly the directions in which secondary electrons are ejected and the form of the probe will play a significant role in determining the measured cross section in a secondary electron imaging experiment.

B. Double-differential cross section

Integrating over the full solid angle $\Omega_{k'}$, to take into account all possible scattering directions of the scattered fast electron allows us to make the so-called *local* approximation for the effective potential¹⁷

$$W(\mathbf{r}_\perp, \mathbf{r}'_\perp) \approx 2V'(\mathbf{r}_\perp)\delta(\mathbf{r}_\perp - \mathbf{r}'_\perp), \quad (6)$$

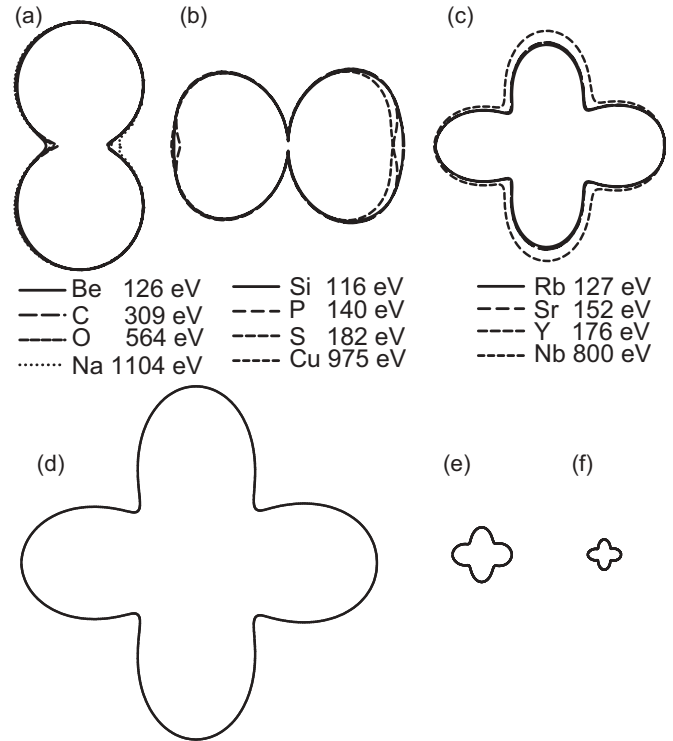


FIG. 6. Normalized double-differential cross sections for the ionization involving (a) 1*s*, (b) 2*p*, and (c) 3*d* electrons for different atoms at 10 eV above the respective ionization thresholds. Also shown are the differential cross sections for ionization involving barium 4*d* electrons for (d) 10-eV above threshold, (e) 50-eV above threshold, and (f) 100-eV above threshold, (d)–(f) are shown on a common scale showing the relative likelihood of electrons being ejected at that energy and direction. In all cases the 200-keV primary electron is incident from the left and we have assumed plane wave illumination. The threshold energies for ionization predicted by the model are shown in parts (a)–(c).

where

$$V'(\mathbf{r}_\perp) = \sum_{\mathbf{g}} W_{\mathbf{g},0} e^{2\pi i \mathbf{g} \cdot \mathbf{r}_\perp}. \quad (7)$$

A double-differential cross section may then be expressed as

$$\left. \frac{d^2\sigma}{d\Omega_{k'} k'^2 dk'} \right|_{\mathbf{R}} = \frac{2\pi t}{h\nu} \int_{\Omega_{k'}} \int_A |\phi_0(\mathbf{R}, \mathbf{r}_\perp, z)|^2 \times \sum_{\mathbf{g}} W_{\mathbf{g},0} e^{2\pi i \mathbf{g} \cdot \mathbf{r}_\perp} d\mathbf{r}_\perp d\Omega_{k'}. \quad (8)$$

An evaluation of Eq. (8) produces the cross sections shown in Fig. 6(a) for the 1*s* electrons for several atoms, Fig. 6(b) the 2*p* electrons for several atoms, and Fig. 6(c) the 3*d* electrons for yet another set of atoms. For the purposes of comparison the cross sections have had their maxima normalized to unity in each case. The orientation of the distribution in Fig. 6(a) relative to the incident direction can be understood on the basis of the discussion of Fig. 4 in Sec. II A, where a significant rotation of the angular distribution even for small scattering angles was noted. Here we are integrating over the full range of scattering angles. We note the similarity in shape for the cross sections for ionization from a state with the same initial angular

momentum. Ionization involving the $4d$ electrons in barium is shown for different energies E_κ of the ejected electrons in Figs. 6(d), 6(e), and 6(f). The shape of the differential cross section does not change significantly from the $3d$ results in Fig. 6(c). All three plots are on the same scale so the relative abundance of the ejected electrons at these different energies above threshold can be deduced. As the energy of the ejected electron above the ionization threshold increases the probability of ionization decreases. This is consistent with the results of Zhu *et al.*,⁵ where the number of detected electrons falls off with increasing secondary electron energy. This suggests that we can assume a relatively unchanging shape, albeit scaled, as the energy of the ejected electron increases.

C. Integration over the single-differential cross section

Integrating up over the range of possible k' determined by the threshold energy for the ionization edge under consideration we obtain

$$\frac{d\sigma}{d\Omega_\kappa} \Big|_{\mathbf{R}} = \frac{2\pi t}{h\nu} \int_{\Omega_{k'}} \int_{k'} \int_A |\phi_0(\mathbf{R}, \mathbf{r}_\perp, z)|^2 \times \sum_{\mathbf{g}} W_{\mathbf{g},0} e^{2\pi i \mathbf{g} \cdot \mathbf{r}_\perp} d\mathbf{r}_\perp k'^2 dk' d\Omega_{k'}. \quad (9)$$

As we have seen above, the distribution of electrons ejected due to inner-shell ionization is largely a function of the angular momentum quantum number of the electrons being ionized and the form of the probe incident on the atom. In a secondary electron imaging experiment, electrons ejected in the backwards direction are those most likely to exit the entrance surface and be detected. We will adopt the approach of integrating up over the probability of ejection in the backwards direction, taking into account an angular-dependent absorption of the ejected electrons, to scale the contributions to the secondary electron imaging contrast for different electrons in different atoms.

As was demonstrated by the results of Zhu *et al.*,⁵ secondary electrons must be emitted close to the crystal entrance surface for them to escape and be detected and this means that secondary electron imaging is restricted to the layers near the surface of the specimen. To be able to accurately simulate secondary electron images this needs to be taken into account. Some form of depth dependence must be included in the expression for the cross section. The importance of accounting for the directional distribution of the ejected electrons to reproducing image contrast in secondary electron imaging is obvious from an inspection of Figs. 5 and 6. Electrons ejected in the backwards direction will have different path lengths to the exit surface. Generalizing an approach suggested by Sternglass²⁰ and more recently by Howie⁶ we write the probability that the secondary electron escapes from the crystal surface, referring to Fig. 7, as

$$P(z) = 0.5 \exp \left[-\frac{r(\theta)}{l(E_\kappa)} \right] = 0.5 \exp \left[-\frac{z}{l(E_\kappa) \cos \theta_\kappa} \right], \quad (10)$$

in terms of an angle-dependent and energy-dependent attenuation factor which is expressed in terms of a mean free

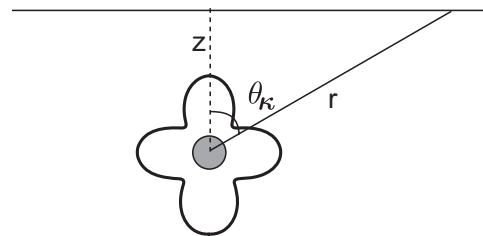


FIG. 7. An electron is ejected at a depth z below the surface at an angle θ and must travel a distance r to escape the crystal.

path for absorption $l(E_\kappa)$, where E_κ is the energy of the ejected electron. The (assumed) factor of 0.5 reflects the probability of an electron wave leaving the crystal surface.²⁰ This approach does not account in detail for the transmission of the ejected electron through the specimen or escape processes. However, we concur with the view of Inada *et al.*⁷ that atomic scale images are unlikely to be significantly influenced by the generation of further secondary electrons through, for example, plasmon decay or cascade processes.

This escape probability is then included when integrating Eq. (9) over the backwards direction as follows:

$$2\pi \int_{-\pi/2}^{\pi/2} \frac{d\sigma}{d\Omega_\kappa} \Big|_{\mathbf{R}} \exp \left[-\frac{z}{l(E_\kappa) \cos \theta_\kappa} \right] d\Omega_\kappa. \quad (11)$$

There are issues to be borne in mind when using a simple attenuation factor to model escape depth, including the lack of available data for inelastic mean free paths at energies below 50 eV. Furthermore, the electron mean free path is strongly dependent on electron energy and it is incorrect to assume that all secondary electrons will be attenuated a similar amount. Higher-energy secondary electrons are less likely to be reabsorbed into the crystal than lower-energy secondary electrons.

To speed up the calculations discussed in the next section, we make the assumption that the shape of the double-differential cross section does not change much with energy loss, as borne out by the results in Figs. 6(d)–6(f). Using Eq. (11) in Eq. (9) we obtain the following description of secondary electron imaging:

$$\sigma_{\text{SE}} \Big|_{\mathbf{R}} = \frac{4\pi^2 t}{h\nu} \int_{k'} \int_A \int_{-\pi/2}^{\pi/2} |\phi_0(\mathbf{R}, \mathbf{r}_\perp, z)|^2 \times \sum_{\mathbf{g}} W_{\mathbf{g},0} e^{2\pi i \mathbf{g} \cdot \mathbf{r}_\perp} \exp \left[-\frac{z}{l(E_\kappa) \cos \theta_\kappa} \right] \times d\Omega_\kappa d\mathbf{r}_\perp k'^2 dk'. \quad (12)$$

III. CASE STUDY: YTTRIUM BARIUM COPPER OXIDE

In the simulations presented in the following sections we use a Bloch wave model to account for the channeling of the probe in the crystal.^{18,21,22} All simulations assumed the following microscope parameters: an aperture of 1.167 \AA^{-1} (an acceptance half-angle of 28 mrad), and a probe accelerating voltage of 200 kV, in accordance with the experiment of Zhu *et al.*⁵ The effect of a finite source size has been included in simulations and has been modeled by convolving the images with a Gaussian having a full-width at half-maximum of 1 \AA .²³

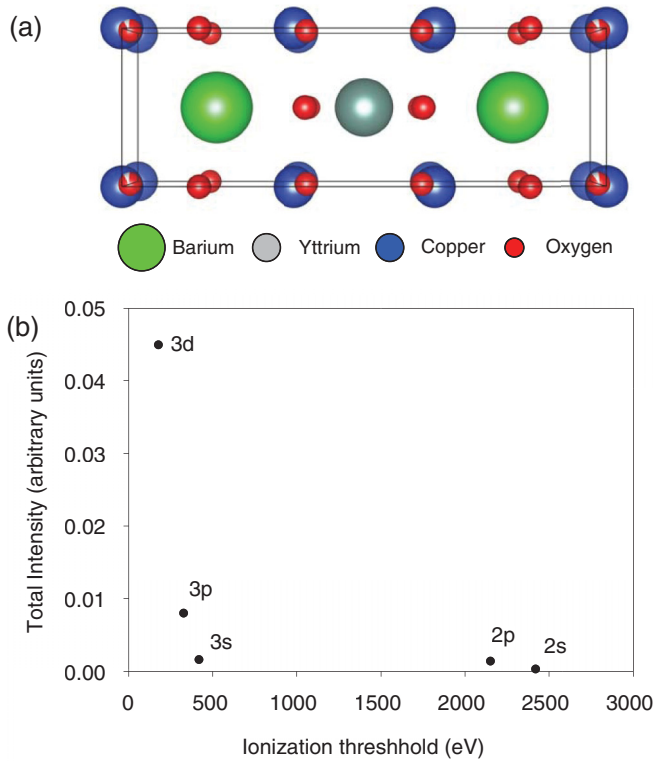


FIG. 8. (Color online) (a) The model structure unit cell of an YBCO specimen oriented along the $\langle 001 \rangle$ zone axis. (b) Total ionization signal for different subshells of yttrium. The 200-keV STEM probe convergence semi-angle was 28 mrad and the crystal was one unit cell thick.

The YBCO crystal parameters used in the simulation were taken from the International Crystallographic Database²⁴ and a model of the unit cell is shown in Fig. 8(a). We have assumed a mean free path for absorption of $l = 4.665 \text{ \AA}$ for the YBCO crystal which was taken from the NIST database²⁵ for an electron energy of 50 eV and this was extrapolated to lower energies assuming that $l(E_\kappa) \propto E_\kappa^{1/2}$ in Eq. (10). The specimen was assumed to be 50- \AA thick.

A. Contribution from different shells

An issue that must be given due thought in the simulation of secondary electron imaging is what electrons in the atoms should be taken into account in the calculation of image contrast. The probability density for wave functions of electrons with low binding energies tends to be delocalized from the atomic positions. They are therefore more affected by the surrounding crystal structure and are often in the valence bands of the crystal. The valence bands produce a diffuse background to secondary electron images and do not provide atomic resolution information. We have not included electrons with a threshold energy of below 85 eV in the following calculations.

Displayed in Fig. 8(b) is the simulated cross section for ionization from different orbitals of the yttrium atom arranged in order of increasing threshold energy. This simulation assumed a scanning transmission electron microscopy (STEM) probe as described in the previous section, and a crystal one unit cell thick. We note a sharp drop in the secondary electron yield

with increasing ionization energy of the subshell. One should also bear in mind that the contribution that a subshell makes also depends on the number of electrons contained within that subshell. The dominant contribution to the secondary electron image comes from the $3d$ and $3p$ electrons in yttrium (10 and 6 electrons, respectively). Similarly the subshells which, in addition, make a significant contribution to the secondary electron signal in YBCO are found to be the barium $3d$ and $4d$ subshells, the copper $2s$, $2p$, and $3p$ subshells and the oxygen $1s$ subshell.

B. Simulation results

We begin our image simulations making the assumption that the direction in which secondary electrons are emitted has little effect on image contrast. Consequently, we integrate Eq. (1) over the full solid angle of the ejected electron, $d\Omega_\kappa$, in effect we are assuming isotropic emission. We obtain the results shown in Fig. 9(a). The specimen was assumed to be

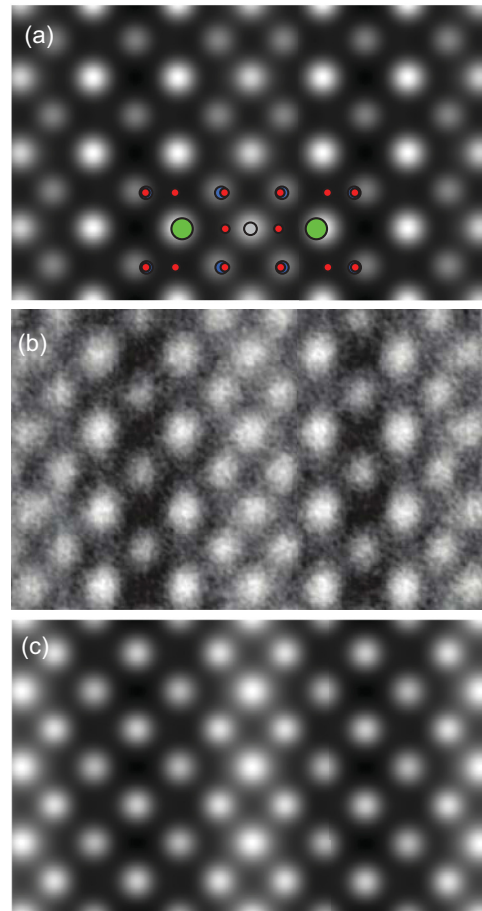


FIG. 9. (Color online) Images of a YBCO specimen where (a) the simulated image assumes a uniform angular distribution of ejected electrons, (b) the experimental image taken by Zhu *et al.* (Ref. 5), and (c) the simulated image, taking into account the differential cross section. The absorption of the secondary electrons is modeled as (a) having no angular dependence, Eq. (10) with $\theta_\kappa = 0$, and (c) using a variable angular dependence. The 200-keV probe with a convergence semi-angle of 28 mrad was modeled as per the description in the text. Simulations assumed a specimen thickness of 50 \AA and a finite source size of FWHM 1.0 \AA .



FIG. 10. The cross section for a single isolated yttrium atom for ionization resulting in an ejected electron energy of (a) 0–6.25, (b) 18.75–25, and (c) 43.75–50 eV. The 200-keV probe with a convergence semi-angle of 28 mrad was modeled as per the description in the text. All images have been normalized to the same scale.

50-Å thick and we applied a depth-dependent attenuation of the cross section according to Eq. (10) for a fixed path length with $\theta_k = 0$. The contribution to the signal for depths greater than 50 Å was negligible. The experimental results of Zhu *et al.* are shown in Fig. 9(b) for comparison.

The contrast in the simulated images qualitatively matches the experimental results with respect to atomic column locations. However, the white bands seen in the vicinity of the yttrium atoms and the intensity on the copper atoms is less bright than in the experimental image, despite this isotropic model being considerably more sophisticated in its treatment of inelastic scattering (ionization) than that of Wu *et al.*⁸ It was postulated by Zhu *et al.*⁵ that the white bands present in the experimental secondary electron image Fig. 9(b), but not in the simulation Fig. 9(a), are a result of the signal from oxygen. The simulation in Fig. 9(a) suggests that this is not the case as the oxygen signal is very weak and does not appear to be the source of the experimental white bands.

We now use the model encapsulated in Eq. (11) and which includes the angular dependence of the ejected electrons after ionization and also an angular-dependent absorption of these electrons. This result is shown in Fig. 9(c). Immediately obvious is the white band near the yttrium atoms providing a better qualitative match to the experimental results in Fig. 9(b). It was hypothesized by Zhu *et al.*⁵ that the white bands present around the yttrium columns were a result of the oxygen columns that are present either side of the yttrium column. However, we see that the white bands come about by a diffuseness in the signal from yttrium. This is caused by the inclusion in Eq. (11) of an energy-dependent attenuation, where the ionization of yttrium resulting in a higher energy of the ejected electron produces a more diffuse cross section, as is shown in Fig. 10. The higher-energy ejected electrons are more likely to escape the crystal and be seen by the detector and this has the net effect of making the yttrium signal appear more diffuse. The second key difference between Figs. 9(a) and 9(c) is that the copper atoms appear brighter in Fig. 9(c) and this is in better agreement with the experimental results. This is because, as was seen in Fig. 5(b), the ionization involving electrons in p orbitals results in the majority of the secondary electrons being ejected in directions roughly parallel to that of the incident electron. This means that a greater proportion of the secondary electrons ejected from copper will be detected because it is the copper $2p$ and $3p$ electrons that provide the dominant signal in the secondary electron YBCO images at that atomic column position.

C. Role of thermally (Rutherford) backscattered electrons

Zhu *et al.*⁵ found that approximately 10% of the electrons had an energy higher than 50 eV and designated these

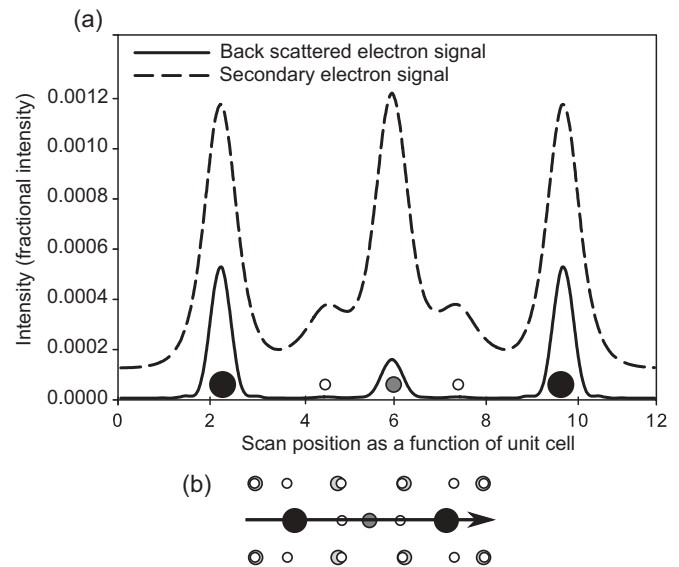


FIG. 11. (a) The intensity for a line scan along the YBCO unit cell passing over the barium (black, $Z = 56$), yttrium (dark gray, $Z = 39$), and oxygen (white, $Z = 8$) atoms. (b) A schematic of the YBCO unit cell showing the direction and position of the linescan (copper atoms, $Z = 29$) are indicated by light gray circles. The secondary electron signal was calculated assuming isotropic emission and assuming a fixed path length for absorption [in Eq. (10) we have $\theta_k = 0$]. The 200-keV probe with a convergence semi-angle of 28 mrad was modeled as per the description in the text. Simulations assumed a specimen thickness of 50 Å and the effect of a finite source size was not taken into account.

backscattered electrons. As discussed, this includes Auger electrons as well as thermally (Rutherford) backscattered electrons.¹² Here we briefly investigate what effect thermally backscattered electrons might have on imaging contrast. Backscattered electrons are significantly higher in energy compared to secondary electrons (which are the result of ionization) and hence they can escape from greater depths within the crystal, bringing information from the bulk of the sample. Backscattering involves the interaction not only between the incident electron and the bound atomic electrons but also the nucleus. Thus the interaction is more closely localized to the position of the atoms within the unit cell.²⁶ Zhu *et al.* were able to remove the secondary electrons originating from ionization events from the measured signal by applying a bias that halted low-energy electrons. The resulting image of the backscattered electrons may then be subtracted from the total image (including secondary electrons) to produce the secondary electron maps.

Nevertheless, we investigate the effect that backscattered electrons may, if not removed, have on the secondary electron image contrast. The backscattering cross section was simulated for the YBCO specimen and a comparison showing the relative signal strengths for the backscattered and secondary electrons is shown in Fig. 11. As expected the total backscattered flux is small in comparison to that from secondary electrons. However, it is strongly localized around the heavy atoms and only barium, the heaviest atom with an atomic number $Z = 56$, has a significant backscattered signal. Oxygen by comparison, with an atomic number $Z = 8$, has a barely noticeable signal.

We conclude that the backscattered contribution will have a small effect on the overall contrast of the image.

IV. SUMMARY

Atomic resolution secondary electron imaging was recently achieved by Zhu *et al.*⁵ In this paper we have developed a quantum mechanical model to understand the images, with the assumption that the contrast is mainly due to electrons ejected in ionization events. In particular, we considered the angular probability distributions of the electrons ejected in the ionization events. The angular distributions were most strongly influenced by the bound state angular momentum quantum number. This model allowed us to match in detail features in the experimental data of Zhu *et al.*⁵ A modest number of atomic orbitals were required to understand the

image contrast. Electrons with too low an ionization threshold were not included as these electrons, often part of the valence band, only contribute a uniform background. Those with a large ionization threshold were only responsible for a small fraction of the signal.

Finally we note that coincidence experiments where only secondary electrons corresponding to fast electrons detected at a given angle are recorded, while being technically more complicated, could uncover interesting physics.

ACKNOWLEDGMENTS

This research was supported under the Discovery Projects funding scheme of the Australian Research Council (Project No. DP110102228). The authors would like to thank Nathan Lugg for several helpful discussions.

*lja@unimelb.edu.au

¹A. V. Crewe, J. Wall, and J. Langmore, *Science* **168**, 1338 (1970).

²R. Erni, M. D. Rossell, C. Kisielowski, and U. Dahmen, *Phys. Rev. Lett.* **102** (2009).

³P. D. Nellist, M. F. Chrisholm, N. Dellby, O. L. Kirivanek, M. F. Murfitt, Z. S. Szilagy, A. R. Lupini, A. Borisevich, W. H. Sides, Jr., and S. J. Pennycook, *Science* **305** (2004).

⁴K. Urban, B. Kabius, M. Haider, and H. Rose, *J. Electron Microsc.* **48**, 821 (1999).

⁵Y. Zhu, H. Inada, K. Nakamura, and J. Wall, *Nat. Mater.* **8**, 808 (2009).

⁶A. Howie, *J. Microsc.* **180**, 192 (1995).

⁷H. Inada, D. Su, R. F. Egerton, M. Konno, L. Wu, J. Ciston, J. Wall, and Y. Zhu, *Ultramicroscopy* **111**, 865 (2011).

⁸L. Wu, R. F. Egerton, and Y. Zhu, *Ultramicroscopy* **123**, 66 (2012).

⁹O. C. Wells and D. C. Joy, *Surf. Interface Anal.* **38**, 1738 (2006).

¹⁰S. Myhajlenko, A. S. Luby, A. M. Fischer, F. A. Ponce, and C. Tracy, *Scanning* **30**, 310 (2008).

¹¹H. Kazumori, K. Honda, M. Matsuya, M. Date, and C. Nielsen, *Microscopy and Microanalysis* **10**(Suppl. S02), 1370 (2004).

¹²H. Seiler, *J. Appl. Phys.* **54**, R1 (1983).

¹³M. Kotera, *J. Appl. Phys.* **65**, 3991 (1989).

¹⁴R. Ramachandra, B. Griffin, and D. Joy, *Ultramicroscopy* **109**, 748 (2009).

¹⁵D. Drouin, A. R. Couture, D. Joly, X. Tastet, V. Aimez, and R. Gauvin, *Scanning* **29**, 92 (2007).

¹⁶A. Lahmam-Bennani, *J. Electron Spectrosc. Relat. Phenom.* **123**, 356 (2002).

¹⁷S. D. Findlay, M. P. Oxley, and L. J. Allen, *Microscopy and Microanalysis* **14**, 48 (2008).

¹⁸M. P. Oxley and L. J. Allen, *Phys. Rev. B* **57**, 3273 (1998).

¹⁹R. D. Cowan, *The Theory of Atomic Structure and Spectra* (University of California Press, Berkeley, CA, 1981).

²⁰E. J. Sternglass, *Phys. Rev.* **108**, 1 (1957).

²¹L. J. Allen, S. D. Findlay, M. P. Oxley, and C. J. Rossouw, *Ultramicroscopy* **96**, 47 (2003).

²²S. D. Findlay, L. J. Allen, M. P. Oxley, and C. J. Rossouw, *Ultramicroscopy* **96**, 65 (2003).

²³P. D. Nellist and J. M. Rodenburg, *Ultramicroscopy* **54**, 61 (1994).

²⁴A. Williams, G. H. Kwei, R. B. Von Dreele, A. C. Larson, I. D. Raistrick, and D. L. Bish, *Phys. Rev. B* **37**, 7960 (1988).

²⁵*NIST Electron Effective-Absorption-Length Database - Version 1.3*, edited by C. J. Powell and A. Jablonski (National Institute of Standards and Technology, Gaithersburg, MD, 2011).

²⁶M. J. Whelan, *J. Appl. Phys.* **36**, 2103 (1965).